

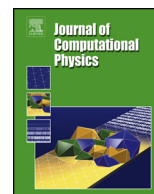


ELSEVIER

Contents lists available at ScienceDirect

Journal of Computational Physics

www.elsevier.com/locate/jcp



An immersed boundary method for simulating Newtonian vesicles in viscoelastic fluid

Yunchang Seol^{a,*}, Yu-Hau Tseng^b, Yongsam Kim^c, Ming-Chih Lai^a^a Department of Applied Mathematics, National Chiao Tung University, 1001 Ta Hsueh Road, Hsinchu 30010, Taiwan^b Department of Applied Mathematics, National University of Kaohsiung, Kaohsiung 81148, Taiwan^c Department of Mathematics, Chung-Ang University, Dongjak-Gu, Heukseok-Dong 221, Seoul 156-175, South Korea

ARTICLE INFO

Article history:

Received 27 March 2018

Received in revised form 27 August 2018

Accepted 18 October 2018

Available online 22 October 2018

Keywords:

Viscoelasticity

Oldroyd-B fluid

Vesicle

Tank-treading

Tumbling

Immersed boundary method

ABSTRACT

In this paper, a two-dimensional immersed boundary method is developed to simulate the dynamics of Newtonian vesicle in viscoelastic Oldroyd-B fluid under shear flow. The viscoelasticity effect of extra stress is well incorporated into the immersed boundary formulation using the indicator function. Our numerical methodology is first validated in comparison with theoretical results in purely Newtonian fluid, and then a series of numerical experiments is conducted to study the effects of different dimensionless parameters on the vesicle motions. Although the tank-treading (TT) motion of Newtonian vesicle in Oldroyd-B fluid under shear flow can be observed just like in Newtonian fluid, it is surprising to find that the stationary inclination angle can be negative without the transition to tumbling (TB) motion. Moreover, the inertia effect plays a significant role that is able to turn the vesicle back to positive inclination angle through TT-TB-TT transition as the Reynolds number increases. To the best of our knowledge, this is the first numerical work for the detailed investigations of Newtonian vesicle dynamics suspended in viscoelastic Oldroyd-B fluid. We believe that our numerical results can be used to motivate further studies in theory and experiments for such coupling vesicle problems.

© 2018 Elsevier Inc. All rights reserved.

1. Introduction

A vesicle is a closed phospholipid membrane, separating the inner fluid from the outer medium. Its typical size is an order of 10 μm , so the dimensionless Reynolds number with typical shear rate less than 10 Hz is about 10^{-3} in water. So far, the experiments of vesicle have been conducted in purely Newtonian fluid, where Newtonian vesicles are suspended in surrounding Newtonian fluids. In general, vesicles mimic the red blood cells (RBCs), and the blood containing RBCs exhibits non-Newtonian properties such as viscoelasticity, shear-thinning, thixotropy, and yield stress [9,39,40]. Motivated from this, we here study the viscoelastic fluid effect on two-dimensional vesicle dynamics under shear flow. An Oldroyd-B fluid model is adopted to account the viscoelasticity, and an immersed boundary (IB) method is developed to simulate primarily the viscoelastic effect on a Newtonian vesicle interacting with surrounding Oldroyd-B fluid in two-phase flows, although our method is not only restricted to this type of fluid.

For the past two decades, three types of vesicle motions under shear flow have been widely studied, namely tank-treading, tumbling, and vacillating-breathing (or trembling, swinging). Those motions can be characterized by the so-called

* Corresponding author.

E-mail addresses: ykseol@math.nctu.edu.tw (Y. Seol), yhtseng@nuk.edu.tw (Y.-H. Tseng), kimy@cau.ac.kr (Y. Kim), mclai@math.nctu.edu.tw (M.-C. Lai).

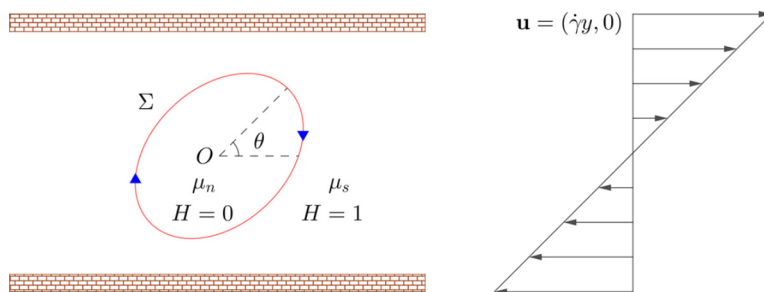


Fig. 1. Simulation setup of a Newtonian vesicle in Oldroyd-B fluid under shear flow denoted by N/O fluid. The vesicle is filled with a Newtonian fluid (viscosity μ_n) while the Oldroyd-B fluid is a mixture of polymer (viscosity μ_p) and Newtonian solvent (viscosity μ_s). The angle θ in radians denotes the inclination angle of the vesicle.

reduced area of vesicle configuration, the viscosity contrast between inner and outer fluids, and the capillary number associated with membrane bending rigidity. So, by carefully controlling these dimensionless parameters, extensive studies were presented in theories [21,29,25], experiments [18,20,10], and simulations [24,47,4,11,5], just to name a few. Refer [1] and references therein for a review of vesicle rheology. Recently, the inertia effect in finite Reynolds number flow becomes a popular research subject as well [23,36,27].

Among many numerical methods, the IB (or front-tracking) method is quite useful for biological problems to simulate a flexible structure interacting with surrounding bulk fluid. There are various extensions of IB method to model vesicles or RBCs dynamics in purely Newtonian fluid [22,26,14,45,15,37,35]. Another extension incorporates a richer fluid such as the Oldroyd-B fluid to study the viscoelastic effect on droplet dynamics [38,8,30,17]. There exists some numerical methods to study droplet dynamics in multiphase viscoelastic flow. In [7], the volume-of-fluid (VOF) method is employed to investigate a droplet deformation under shear flow. The level-set method in [33] and the front-tracking method in [17] are employed to study a droplet in buoyancy- and pressure-driven flows. In these studies, the multiphase viscoelastic flow is accomplished by varying the parameter of polymer relaxation time (or the dimensionless Weissenberg number) in the polymer stress evolution equation. In this framework, a smoothed indicator function multiplied to the parameter is close to zero in the region of Newtonian phase, which is problematic when solving the equation. To circumvent this difficulty, the diffuse interface (or phase-field) method proposed in [46] to study Newtonian droplet suspended in an Oldroyd-B fluid under creeping shear flow adopts a different approach; that is, the time evolution of polymer stress equation is solved on the entire domain first and then the extra polymer stress is added back to the viscoelastic region via the phase field function. Here, following the similar idea of handling the extra stress part in [46], we develop an immersed boundary method for simulating the dynamics of Newtonian vesicle in an Oldroyd-B fluid which also takes the viscosity contrast and inertia effect into account. To the best of our knowledge, it seems to be the first numerical work on this coupling flow problem. Two major interesting findings are briefed here. Firstly, the tank-treading motion of Newtonian vesicle in Oldroyd-B fluid under shear flow can be observed just like in Newtonian fluid. However, as we increase the Weissenberg number, the stationary inclination angle can be negative without the transition to tumbling motion. Secondly, by increasing the inertia effect on the unmatched viscosity contrast case, the tank-treading motion with negative inclination angle can turn into the same motion but with positive inclination angle. The interplay between the viscoelasticity and the inertia is interesting and worths further investigations.

The rest of this paper is organized as follows. In next section, we present the governing equations based on the immersed boundary framework which describe the two-phase flow consisting of a Newtonian vesicle in an Oldroyd-B fluid. In Section 3, we transform the equations into dimensionless form and outline the time-stepping algorithm for solving the whole fluid system. To verify our code implementation, numerical accuracy test for an Oldroyd-B fluid solver is conducted as well. In Section 5, a series of numerical experiments is conducted to study the effects of different dimensionless parameters on the Newtonian vesicle dynamics under shear flow in an Oldroyd-B fluid. Conclusions and future work are given in Section 6.

2. Mathematical model

In this paper, we consider an immiscible two-phase flow consisting of a Newtonian vesicle in an Oldroyd-B fluid under shear flow in a two-dimensional domain Ω as depicted in Fig. 1. The vesicle boundary Σ separating those two fluids is assumed to be a closed smooth curve immersed in Ω . The model is formulated by the immersed boundary method in which the fluid parts in different regions use different models (Newtonian or Oldroyd-B) and the vesicle effect is termed as the elastic tension and bending force along the vesicle boundary. Certainly, those forces are derived by the energy law defined on the vesicle boundary described in literature. Meanwhile, there are related energy laws to describe the viscoelastic effect of fluids such as phase-field method developed in [46]. Based on the phase-field variable and its gradient, the mixing energy can be represented by Ginzburg–Landau form which produces the interfacial tension force between two phases. The extra stress for polymer contribution in an Oldroyd-B fluid can be derived from the dumbbell elastic energy through a variational procedure. By adding the viscous stress of surrounding fluid, the total stress tensor is the sum of those three

terms. The fluid velocity $\mathbf{u}(\mathbf{x}, t)$ and pressure $p(\mathbf{x}, t)$ are described in Eulerian manner while the vesicle boundary $\mathbf{X}(\alpha, t)$ is described in Lagrangian manner, so the governing equations of this two-phase flow can be written in a single fluid system as follows.

$$\rho \left(\frac{\partial \mathbf{u}}{\partial t} + (\mathbf{u} \cdot \nabla) \mathbf{u} \right) = -\nabla p + \nabla \cdot [((1 - H)\mu_n + H\mu_s) \mathbb{D}(\mathbf{u}) + H\sigma] + \mathbf{f} \text{ in } \Omega, \tag{1}$$

$$\nabla \cdot \mathbf{u} = 0 \text{ in } \Omega, \tag{2}$$

$$\mathbf{f}(\mathbf{x}, t) = \int_{\Sigma} (\mathbf{F}_\gamma + \mathbf{F}_b)(\alpha, t) \delta(\mathbf{x} - \mathbf{X}(\alpha, t)) |\mathbf{X}_\alpha| \, d\alpha \text{ in } \Omega, \tag{3}$$

$$\frac{\partial \mathbf{X}}{\partial t}(\alpha, t) = \mathbf{U}(\alpha, t) = \int_{\Omega} \mathbf{u}(\mathbf{x}, t) \delta(\mathbf{x} - \mathbf{X}(\alpha, t)) \, d\mathbf{x} \text{ on } \Sigma, \tag{4}$$

$$\gamma(\alpha, t) = \gamma_0 \left(\frac{|\mathbf{X}_\alpha(\alpha, t)|}{|\mathbf{X}_\alpha(\alpha, 0)|} - 1 \right) \text{ on } \Sigma, \tag{5}$$

$$\mathbf{F}_\gamma(\alpha, t) = \frac{1}{|\mathbf{X}_\alpha|} \frac{\partial(\gamma\tau)}{\partial\alpha}, \quad \mathbf{F}_b(\alpha, t) = c_b \left(\kappa_{ss} + \frac{\kappa^3}{2} \right) \mathbf{n} \text{ on } \Sigma, \tag{6}$$

$$\overset{\nabla}{\xi} \sigma + \sigma = \mu_p \mathbb{D}(\mathbf{u}) \text{ in } \Omega, \tag{7}$$

where

$$\overset{\nabla}{\sigma} = \frac{\partial \sigma}{\partial t} + \mathbf{u} \cdot \nabla \sigma - (\nabla \mathbf{u} \sigma + \sigma (\nabla \mathbf{u})^T), \tag{8}$$

$$\mathbb{D}(\mathbf{u}) = \nabla \mathbf{u} + (\nabla \mathbf{u})^T, \quad \nabla \mathbf{u} = \begin{bmatrix} u_x & u_y \\ v_x & v_y \end{bmatrix}. \tag{9}$$

Eqs. (1) and (2) are the Navier–Stokes equations in which H is the indicator (or Heaviside) function defined by

$$H(\mathbf{x}, t) = \begin{cases} 1 & \text{if } \mathbf{x} \text{ is in Oldroyd-B fluid,} \\ 0 & \text{if } \mathbf{x} \text{ is in Newtonian vesicle.} \end{cases} \tag{10}$$

Here we assume both fluids have the same constant density denoted by ρ , whereas the Newtonian fluid viscosity μ_n and the Oldroyd-B fluid viscosity may be different. The Newtonian solvent viscosity μ_s and the polymer viscosity μ_p determine the total viscosity of Oldroyd-B fluid, see Fig. 1. The extra stress σ contributes the viscoelasticity to the Navier–Stokes equations only in the Oldroyd-B fluid part where $H(\mathbf{x}, t) = 1$. In Eq. (3), the Eulerian force \mathbf{f} arises from the spreading of interfacial force \mathbf{F} via the Dirac delta function $\delta(\mathbf{x}) = \delta(x)\delta(y)$. Similarly, as shown in Eq. (4), the interfacial velocity \mathbf{U} is interpolated from the local Eulerian fluid velocity via the delta function. Here the inextensible vesicle boundary is relaxed by the nearly inextensible approach in which a spring-like tension given in Eq. (5) is introduced. This approach is motivated from the equality $\partial|\mathbf{X}_\alpha|/\partial t = |\mathbf{X}_\alpha| \nabla_s \cdot \mathbf{U}$ and has been validated to be effective for applications under various flows in 2D [3], axisymmetric case [15], and 3D [35]. The interfacial force in Eq. (6) consists of two components; namely, the tension force \mathbf{F}_γ and the bending force \mathbf{F}_b . In the bending force in Eq. (6), c_b is the bending rigidity constant, κ is the local curvature, and the surface Laplacian of κ is represented by

$$\kappa_{ss} = \frac{1}{|\mathbf{X}_\alpha|} \frac{\partial}{\partial \alpha} \left(\frac{1}{|\mathbf{X}_\alpha|} \frac{\partial \kappa}{\partial \alpha} \right) = \frac{-\mathbf{X}_\alpha \cdot \mathbf{X}_{\alpha\alpha}}{|\mathbf{X}_\alpha|^4} \frac{\partial \kappa}{\partial \alpha} + \frac{1}{|\mathbf{X}_\alpha|^2} \frac{\partial^2 \kappa}{\partial \alpha^2}. \tag{11}$$

The latter expansion formula will be used to enhance the numerical accuracy, refer to Appendix D in [44]. The vesicle boundary $\Sigma(t)$ between two fluids is a one-dimensional curve represented by $\Sigma(t) = \{\mathbf{X}(\alpha, t) = (X(\alpha, t), Y(\alpha, t)) | 0 \leq \alpha < 2\pi\}$, where α is the Lagrangian coordinate. The subscript α of a function denotes its partial derivative of the function with respect to α . We then define the unit tangent vector as $\tau = (\tau_1, \tau_2) = \mathbf{X}_\alpha/|\mathbf{X}_\alpha|$ and the outward unit normal vector as $\mathbf{n} = (\tau_2, -\tau_1)$, where $|\cdot|$ stands for the usual Euclidean norm. So the signed curvature of the curve can be written as $\kappa = (X_\alpha Y_{\alpha\alpha} - Y_\alpha X_{\alpha\alpha}) / (X_\alpha^2 + Y_\alpha^2)^{3/2}$. The extra stress $\sigma(\mathbf{x}, t)$ in Eq. (1) represents the viscoelastic contribution of the Oldroyd-B fluid and is governed by Eq. (7), where the parameter ξ is the polymer relaxation time, $\overset{\nabla}{\sigma}$ is the upper convected time derivative of σ defined in Eq. (8), and $\mathbb{D}(\mathbf{u})$ is the rate of deformation tensor as in Eq. (9). Of course, the above governing equations (1)–(7) should accompany with some suitable initial and boundary conditions which will be described later.

3. Numerical method and accuracy

3.1. Dimensionless governing equations

The governing equations (1)–(7) can be written in the dimensionless form as follows. For a vesicle boundary enclosing an area A with its perimeter L , we define the effective radius of the vesicle $R = \sqrt{A/\pi}$ as the characteristic length scale. The characteristic time scale is defined by $t_c = 1/\dot{\gamma}$, where $\dot{\gamma}$ is the shear rate of flow. Then all physical variables are scaled by the associated characteristic quantities as

$$\mathbf{x}^* = \frac{\mathbf{x}}{R}, \quad t^* = \frac{t}{t_c}, \quad \mathbf{u}^* = \frac{\mathbf{u}}{R/t_c}, \quad p^* = \frac{t_c}{\mu_s} p, \quad \sigma^* = \frac{t_c}{\mu_s} \sigma. \tag{12}$$

After performing substitutions and a few calculations, the dimensionless governing equations for Newtonian vesicle in Oldroyd-B fluid system (N/O fluid) can be written as (dropping the asterisk)

$$Re \left(\frac{\partial \mathbf{u}}{\partial t} + (\mathbf{u} \cdot \nabla) \mathbf{u} \right) = -\nabla p + \nabla \cdot [((1 - H)\lambda + H)\mathbb{D}(\mathbf{u}) + H\sigma] + \mathbf{f} \quad \text{in } \Omega, \tag{13}$$

$$\nabla \cdot \mathbf{u} = 0 \quad \text{in } \Omega, \tag{14}$$

$$\mathbf{f}(\mathbf{x}, t) = \int_{\Sigma} (\mathbf{F}_\gamma + \mathbf{F}_b)(\alpha, t) \delta(\mathbf{x} - \mathbf{X}(\alpha, t)) |\mathbf{X}_\alpha| d\alpha \quad \text{in } \Omega, \tag{15}$$

$$\frac{\partial \mathbf{X}}{\partial t}(\alpha, t) = \mathbf{U}(\alpha, t) = \int_{\Omega} \mathbf{u}(\mathbf{x}, t) \delta(\mathbf{x} - \mathbf{X}(\alpha, t)) d\mathbf{x} \quad \text{on } \Sigma, \tag{16}$$

$$\gamma(\alpha, t) = \gamma_0 \left(\frac{|\mathbf{X}_\alpha(\alpha, t)|}{|\mathbf{X}_\alpha(\alpha, 0)|} - 1 \right) \quad \text{on } \Sigma, \tag{17}$$

$$\mathbf{F}_\gamma(\alpha, t) = \frac{1}{|\mathbf{X}_\alpha|} \frac{\partial(\gamma \boldsymbol{\tau})}{\partial \alpha}, \quad \mathbf{F}_b(\alpha, t) = \frac{1}{Ca} \left(\Delta_s \kappa + \frac{\kappa^3}{2} \right) \mathbf{n} \quad \text{on } \Sigma, \tag{18}$$

$$Wi \overset{\nabla}{\sigma} + \sigma = \beta \mathbb{D}(\mathbf{u}) \quad \text{in } \Omega, \tag{19}$$

where

$$Re = \frac{\rho R^2}{\mu_s t_c}, \quad Ca = \frac{\mu_s R^3}{c_b t_c}, \quad Wi = \frac{\xi}{t_c}, \quad \lambda = \frac{\mu_n}{\mu_s}, \quad \beta = \frac{\mu_p}{\mu_s}. \tag{20}$$

Here, Re is the fluid Reynolds number, the capillary number Ca measures the ratio of viscous force and bending force, and the Weissenberg number Wi measures the ratio of elastic force and viscous force in Oldroyd-B fluid. We also denote λ by the viscosity contrast between the interior Newtonian fluid and the Newtonian solvent of Oldroyd-B fluid, and β by the viscosity contrast between the polymer and the Newtonian solvent. For instance, in a single-phase Newtonian fluid, we set the parameters by $\beta = Wi = 0$ and $\lambda = 1$. Notice that, there is no dimensionless parameter in the righthand side of \mathbf{F}_γ term since it can be absorbed into the stiffness parameter γ_0 which will be chosen later.

3.2. Numerical scheme

We next present the numerical scheme and some related implementation details for solving the dimensionless governing equations (13)–(19). Throughout this paper, the periodic boundary condition is imposed for all physical variables in the x direction, while the Dirichlet and zero Neumann boundary conditions are imposed for the velocity and the extra stress, respectively, in the y direction. To solve the Navier–Stokes equations (13)–(14) in a computational domain $\Omega \subseteq \mathbb{R}^2$, we layout a uniform Cartesian grid with mesh width $h = \Delta x = \Delta y$, and allocate the fluid velocity $\mathbf{u} = (u, v)$ and the pressure p in a staggered marker-and-cell (MAC) grid manner [16]. Expressing the extra polymer stress by

$$\sigma = \begin{bmatrix} \sigma^a & \sigma^b \\ \sigma^b & \sigma^c \end{bmatrix},$$

we allocate the diagonal components, σ^a and σ^c , to the cell center and the off-diagonal component σ^b to the cell corner, so that the divergence form $\nabla \cdot (H\sigma)$ is compatible with the staggered grid associated with fluid velocities as shown in Fig. 2. Those stress grid allocations can be found in the reference [8]. Besides, the indicator function H is defined at the cell center, so when a variable is necessarily shifted by a half-mesh width for relevant computations, the linear interpolation is simply employed. For example, we define

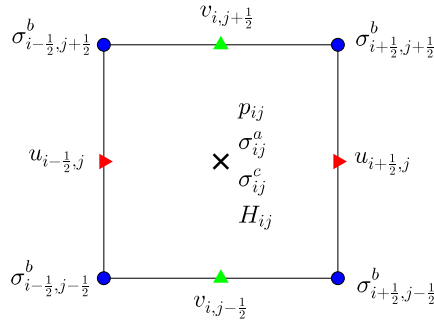


Fig. 2. Grid allocations for fluid variables u, v, p , the extra stress σ , and the indicator function H .

$$\sigma_{i+\frac{1}{2},j}^b = \frac{\sigma_{i+\frac{1}{2},j-\frac{1}{2}}^b + \sigma_{i+\frac{1}{2},j+\frac{1}{2}}^b}{2} \quad \text{and} \quad \sigma_{i,j}^b = \frac{\sigma_{i-\frac{1}{2},j-\frac{1}{2}}^b + \sigma_{i-\frac{1}{2},j+\frac{1}{2}}^b + \sigma_{i+\frac{1}{2},j-\frac{1}{2}}^b + \sigma_{i+\frac{1}{2},j+\frac{1}{2}}^b}{4}.$$

Note that we define a variable at the cell center by $\sigma_{i,j}^b = \sigma^b(x_i, y_i) = \sigma^b(x_0 + (i - 1/2)h, y_0 + (j - 1/2)h)$ due to the use of staggered grid. In the similar fashion, other variables can be linearly interpolated from the values of neighboring points.

For the closed vesicle boundary \mathbf{X} , we use Fourier representation to discretize it as

$$\mathbf{X}(\alpha, t) = \sum_{k=-N/2}^{N/2-1} \widehat{\mathbf{X}}(k, t) e^{ik\alpha}. \tag{21}$$

So the vesicle boundary is represented by a set of Lagrangian markers $\mathbf{X}_\ell = \mathbf{X}(\alpha_\ell)$, where $\alpha_\ell = \ell \Delta\alpha$ and $\Delta\alpha = 2\pi/N$. The associated geometric quantities used in the above formulations such as interface tangent and normal vector, the curvature, and their derivatives are all computed at the Lagrangian markers \mathbf{X}_ℓ using the Fourier spectral differentiations [42]. These spectral derivatives with respect to α can be computed efficiently using Fast Fourier Transform (FFT) in a spectral accuracy. To remove the aliasing error in computations, we adopt the de-aliasing 2/3-rule filter. Due to the inextensibility of vesicle boundary, the Lagrangian markers clustering during the simulations is not that severe comparing with the droplet case. Therefore, we do not employ the markers redistribution technique in present simulations.

We now present how to march the Lagrangian markers $\mathbf{X}^n = \mathbf{X}(n\Delta t)$ from time level n to $\mathbf{X}^{n+1} = \mathbf{X}(n\Delta t + \Delta t)$ at time level $n + 1$ with the time step size Δt . In the following, the polymer stress σ^n , the fluid velocity \mathbf{u}^n , the pressure p^n , and the Lagrangian markers \mathbf{X}^n are all given in advance, and from these variables we aim to update σ^{n+1} , \mathbf{u}^{n+1} , p^{n+1} , and \mathbf{X}^{n+1} . The step-by-step numerical procedure can be done as follows.

Step 1. At the Lagrangian markers \mathbf{X}_ℓ^n , we first compute all the geometric quantities using the spectral differentiations and the spring-like tension by

$$\gamma_\ell^n = \gamma(\mathbf{X}_\ell^n) = \gamma_0 \left(\frac{|\mathbf{X}_{\alpha\alpha}^n|}{|\mathbf{X}_{\alpha\alpha}^0|} - 1 \right),$$

and then incorporate those to compute the interfacial forces

$$\mathbf{F}_\gamma(\mathbf{X}_\ell^n) = \frac{1}{|\mathbf{X}_{\alpha\alpha}^n|} \left(\frac{\partial \gamma \tau}{\partial \alpha} \right)_\ell,$$

$$\mathbf{F}_b(\mathbf{X}_\ell^n) = \frac{1}{Ca} \left(-\frac{(\mathbf{X}_\alpha^n \cdot \mathbf{X}_{\alpha\alpha}^n)(\kappa_\alpha)_\ell^n}{|\mathbf{X}_{\alpha\alpha}^n|^4} + \frac{(\kappa_{\alpha\alpha})_\ell^n}{|\mathbf{X}_{\alpha\alpha}^n|^2} + \frac{(\kappa_\ell^n)^3}{2} \right) \mathbf{n}_\ell^n.$$

Step 2. Distribute the tension and bending forces acting on Lagrangian markers into the Eulerian grid by using the smoothed Dirac delta function δ_h as

$$\mathbf{f}^n(\mathbf{x}) = \sum_{\ell=0}^{N-1} (\mathbf{F}_\gamma(\mathbf{X}_\ell^n) + \mathbf{F}_b(\mathbf{X}_\ell^n)) \delta_h(\mathbf{x} - \mathbf{X}_\ell^n) ds(\mathbf{X}_\ell^n),$$

where $\mathbf{x} = (x, y)$ is the Eulerian grid point and the arc-length element is obtained by $ds(\mathbf{X}_\ell^n) = |\mathbf{X}_{\alpha\alpha}^n| \Delta\alpha$. For the discrete delta function $\delta_h(\mathbf{x}) = \frac{1}{h^2} \phi\left(\frac{x}{h}\right) \phi\left(\frac{y}{h}\right)$, we employ the 6-point supported C^3 function ϕ newly developed in [2].

Step 3. Solve the Navier–Stokes equations by the second-order incremental pressure-correction projection method in [12] as follows.

$$\begin{aligned}
 & Re \left(\frac{3\mathbf{u}^* - 4\mathbf{u}^n + \mathbf{u}^{n-1}}{2\Delta t} + 2(\mathbf{u}^n \cdot \nabla_h) \mathbf{u}^n - (\mathbf{u}^{n-1} \cdot \nabla_h) \mathbf{u}^{n-1} \right) \\
 &= -\nabla_h p^n + \lambda \Delta_h \mathbf{u}^* + \nabla_h \cdot \left[(1 - \lambda) H^n \left(\nabla_h \mathbf{u}^n + (\nabla_h \mathbf{u}^n)^T \right) \right] + \nabla_h \cdot (H^n \sigma^n) + \mathbf{f}^n, \\
 & \Delta_h p^* = \frac{3Re}{2\Delta t} \nabla_h \cdot \mathbf{u}^*, \quad \frac{\partial p^*}{\partial \mathbf{n}} = 0 \text{ on } \partial\Omega_D, \quad \mathbf{u}^* = \mathbf{u}^{n+1} \text{ on } \partial\Omega_D, \\
 & \mathbf{u}^{n+1} = \mathbf{u}^* - \frac{2\Delta t}{3Re} \nabla_h p^*, \quad \nabla_h p^{n+1} = \nabla_h p^* + \nabla_h p^n - \frac{2\lambda\Delta t}{3Re} \Delta_h (\nabla_h p^*),
 \end{aligned}$$

where the discrete operators ∇_h and $\nabla_h \cdot$ approximate the gradient and divergence operators, respectively, using the second-order finite difference in staggered grid. For the nonlinear terms, the skew-symmetric form is employed as $(\mathbf{u} \cdot \nabla_h) \mathbf{u} = \frac{1}{2} (\mathbf{u} \cdot \nabla_h) \mathbf{u} + \frac{1}{2} \nabla_h (\mathbf{u}\mathbf{u})$. The Dirichlet boundary is denoted by $\partial\Omega_D$. The smoothed indicator function H^n can be obtained by solving the discretized Poisson equation, as described in [43],

$$\Delta_h H^n(\mathbf{x}) = \nabla_h \cdot \sum_{\ell=0}^{N-1} \mathbf{n}_\ell^n \delta(\mathbf{x} - \mathbf{X}_\ell^n) ds(\mathbf{X}_\ell^n).$$

The numerical scheme for viscous term written above is suggested when $\lambda \geq 1$, so that the more viscous part is treated implicitly with the constant coefficient λ while the less viscous part is treated explicitly. Therefore, a fast solver using FFT can be implemented directly. Notice that, as the traditional IB method, the interfacial force \mathbf{f}^n is computed explicitly in Step 2 so here the extra stress term is also computed explicitly for the simplicity and compatibility.

Step 4. Once \mathbf{u}^{n+1} is determined in the Eulerian grid points, we interpolate the fluid interfacial velocity $\mathbf{U}_\ell^{n+1} = \sum_{\mathbf{x}} \mathbf{u}^{n+1}(\mathbf{x}) \delta_h(\mathbf{x} - \mathbf{X}_\ell^n) h^2$. Therefore, the Lagrangian markers can be updated by $\mathbf{X}_\ell^{n+1} = \mathbf{X}_\ell^n + \Delta t \mathbf{U}_\ell^{n+1}$.

Step 5. As the last step, we solve the extra stress equation

$$\frac{\partial \sigma}{\partial t} = \mathbb{F}(\sigma, \mathbf{u}),$$

where

$$\mathbb{F}(\sigma, \mathbf{u}) = -\nabla_h \cdot (\mathbf{u}\sigma) + \left(\nabla_h \mathbf{u}\sigma + \sigma (\nabla_h \mathbf{u})^T \right) - \frac{\sigma}{Wi} + \frac{\beta}{Wi} \left(\nabla_h \mathbf{u} + (\nabla_h \mathbf{u})^T \right).$$

Following in [8], we use the second-order Runge–Kutta (RK2) method with zero-Neumann boundary condition at Dirichlet boundary of fluid velocity to update σ^{n+1} . Introducing two intermediate variables σ_1 and σ_2 by

$$\sigma_1 = \sigma^n + \Delta t \mathbb{F}(\sigma^n, \mathbf{u}^n), \quad \sigma_2 = \sigma_1 + \Delta t \mathbb{F}(\sigma_1, \mathbf{u}^{n+1}),$$

the updated extra stress is obtained by $\sigma^{n+1} = (\sigma^n + \sigma_2)/2$. In this computation using RK2 method, we note that all the components of σ are located at cell centers by linear interpolation, and the convection term is written in divergence form due to the identity $\mathbf{u} \cdot \nabla_h \sigma = \nabla_h \cdot (\mathbf{u}\sigma)$.

4. Code verification and validation

We test the convergence rates of single-phase Oldroyd-B fluid solver and immersed boundary method for vesicle dynamics in two-phase N/O fluid. The code validation is also performed by comparison of droplet deformation in N/O fluid.

4.1. Convergence study for single-phase Oldroyd-B fluid

Here, we test the single-phase Oldroyd-B fluid solver presented in the previous section by checking the numerical accuracy of the following analytical solution in a computational domain $\Omega = [0, 2\pi] \times [\pi/2, 5\pi/2]$. The single-phase Oldroyd-B fluid equations are written as

$$Re \left(\frac{\partial \mathbf{u}}{\partial t} + (\mathbf{u} \cdot \nabla) \mathbf{u} \right) = -\nabla p + \Delta \mathbf{u} + \nabla \cdot \sigma \quad \text{in } \Omega, \tag{22}$$

$$\nabla \cdot \mathbf{u} = 0 \quad \text{in } \Omega, \tag{23}$$

$$Wi \overset{\nabla}{\sigma} + \sigma = \beta \mathbb{D}(\mathbf{u}) + \phi \quad \text{in } \Omega, \tag{24}$$

where an auxiliary function ϕ is added in Eq. (24) and defined by

Table 1

Temporal convergence analysis in L_∞ norm for the fluid velocity $\mathbf{u} = (u, v)$, pressure p , and the polymer stress σ at two different times $t = 0.6$ and $t = 1.2$.

M	$\ u_M - u_e\ _\infty$	Rate	$\ v_M - v_e\ _\infty$	Rate	$\ p_M - p_e\ _\infty$	Rate
$(t = 0.6)$						
64	1.287E-02	–	1.173E-02	–	4.270E-02	–
128	6.291E-03	1.03	5.735E-03	1.03	2.181E-02	0.96
256	3.108E-03	1.01	2.833E-03	1.01	1.100E-02	0.98
512	1.544E-03	1.00	1.408E-03	1.00	5.522E-03	0.99
$(t = 1.2)$						
64	9.512E-03	–	8.290E-03	–	3.775E-02	–
128	4.697E-03	1.01	4.091E-03	1.01	1.935E-02	0.96
256	2.334E-03	1.00	2.033E-03	1.00	9.780E-03	0.98
512	1.163E-03	1.00	1.013E-03	1.00	4.914E-03	0.99
M	$\ \sigma_M^a - \sigma_e^a\ _\infty$	Rate	$\ \sigma_M^b - \sigma_e^b\ _\infty$	Rate	$\ \sigma_M^c - \sigma_e^c\ _\infty$	Rate
$(t = 0.6)$						
64	8.391E-02	–	1.035E-02	–	8.508E-02	–
128	4.697E-02	0.99	5.286E-03	0.96	4.234E-02	1.00
256	2.099E-02	1.00	2.661E-03	0.99	2.108E-02	1.00
512	1.049E-02	1.00	1.334E-03	0.99	1.052E-02	1.00
$(t = 1.2)$						
64	4.583E-02	–	1.765E-02	–	4.660E-02	–
128	2.329E-02	0.97	8.937E-03	0.98	2.351E-02	0.98
256	1.173E-02	0.98	4.486E-03	0.99	1.179E-02	0.99
512	5.887E-03	0.99	2.247E-03	0.99	5.903E-03	0.99

$$\phi = Wi \beta \begin{bmatrix} \phi^a & \phi^b \\ \phi^b & \phi^c \end{bmatrix}, \quad G(t) = e^{-2(1+\beta)t/Re},$$

$$\phi^a = -2G' \sin x \sin y - 2G^2 \cos^2 x \sin^2 y + 2G^2 \sin^2 x \cos^2 y - 4G^2 \sin^2 x \sin^2 y,$$

$$\phi^b = -4G^2 \sin x \cos x \sin y \cos y,$$

$$\phi^c = 2G' \sin x \sin y + 2G^2 \cos^2 x \sin^2 y - 2G^2 \sin^2 x \cos^2 y - 4G^2 \sin^2 x \sin^2 y.$$

The prime symbol of G denotes the derivative with respect to time t . After some careful calculations referring to Taylor–Green vortex, one can easily check that the following analytical solution satisfies the above equations (22)–(24).

$$\mathbf{u}_e = (G \cos x \sin y, -G \sin x \cos y), \quad p_e = -\frac{Re}{4}(\cos 2x + \cos 2y)G^2, \tag{25}$$

$$\sigma_e = \beta \mathbb{D}(\mathbf{u}) = \beta \begin{bmatrix} -2G \sin x \sin y & 0 \\ 0 & 2G \sin x \sin y \end{bmatrix}.$$

Table 1 shows the convergence analysis for all solution variables at two different times $t = 0.6$ and $t = 1.2$. We set the parameters by $Re = Wi = \beta = 1$ and $\Delta t = h/8$, where h is the Eulerian mesh width defined by $h = 2\pi/M$ with grid size M . The convergence rate of the fluid velocity u is obtained by

$$\text{Rate} = \log_2(\|u_M - u_e\|_\infty / \|u_{2M} - u_e\|_\infty),$$

and so are the other variables. The numerical results for all variables in Table 1 show clean first-order accuracy due to the explicit treatment of the polymer stress term $\nabla \cdot \sigma$ of Eq. (22) which is described in Step 3. In general, the immersed boundary method is first-order accurate, unless special algorithm is employed for higher-order such as in immersed interface method. Thus, this accuracy behavior is acceptable and consistent with the present IB method. One might want to further extend our method to achieve the second-order accuracy in solving the Oldroyd-B fluid flow by treating the extra stress term in the same way as the nonlinear advection term in projection method of Step 3 in Subsection 3.2. However, we do not adopt this treatment here due to the present immersed boundary method is only first-order accurate when the vesicle boundary force is taken into account. We further verify the spatial convergence of our fluid solver. To do this, smaller time step size is chosen by $\Delta t = h/128$ so that the dominant error mainly arises from the space, while other parameters remain the same. Table 2 confirms that our solver has the second order accuracy in L_2 norm. The solution variables are all defined on staggered grid so when the mesh is refined, the solution locations at coarse and fine grids do not coincide with each other. Hence, the usage of L_2 error instead of L_∞ is a natural choice.

4.2. Convergence study for Newtonian vesicle dynamics in Oldroyd-B fluid

In this subsection, we perform the convergence study to verify the present numerical algorithm for vesicle dynamics in two-phase flow. We put a Newtonian vesicle into Oldroyd-B fluid under shear flow. We choose the vesicle with $\nu = 0.8$

Table 2

Spatial convergence analysis in L_2 norm for the fluid velocity $\mathbf{u} = (u, v)$, pressure p , and the polymer stress σ at two different times $t = 0.6$ and $t = 1.2$.

M	$\ u_M - u_e\ _2$	Rate	$\ v_M - v_e\ _2$	Rate	$\ p_M - p_e\ _2$	Rate
$(t = 0.6)$						
64	2.958E-04	–	2.749E-04	–	5.352E-04	–
128	6.366E-05	2.22	5.981E-05	2.20	1.253E-04	2.09
256	1.466E-05	2.12	1.384E-05	2.11	3.042E-05	2.04
512	3.510E-06	2.06	3.324E-06	2.06	7.501E-06	2.02
$(t = 1.2)$						
64	1.628E-04	–	1.483E-04	–	4.084E-04	–
128	3.982E-05	2.03	3.680E-05	2.01	1.028E-04	1.99
256	9.854E-06	2.01	9.175E-06	2.00	2.587E-05	1.99
512	2.451E-06	2.01	2.291E-06	2.00	6.490E-06	2.00
M	$\ \sigma_M^a - \sigma_e^a\ _2$	Rate	$\ \sigma_M^b - \sigma_e^b\ _2$	Rate	$\ \sigma_M^c - \sigma_e^c\ _2$	Rate
$(t = 0.6)$						
64	9.637E-04	–	1.625E-04	–	9.563E-04	–
128	2.295E-04	2.07	3.554E-05	2.19	2.283E-04	2.07
256	5.597E-05	2.04	8.275E-06	2.10	5.575E-05	2.03
512	1.381E-05	2.02	1.994E-06	2.05	1.377E-05	2.02
$(t = 1.2)$						
64	4.004E-04	–	1.621E-04	–	3.898E-04	–
128	1.012E-04	1.98	3.778E-05	2.10	9.920E-05	1.97
256	2.545E-05	1.99	9.097E-06	2.05	2.504E-05	1.99
512	6.383E-06	2.00	2.230E-06	2.03	6.291E-06	1.99

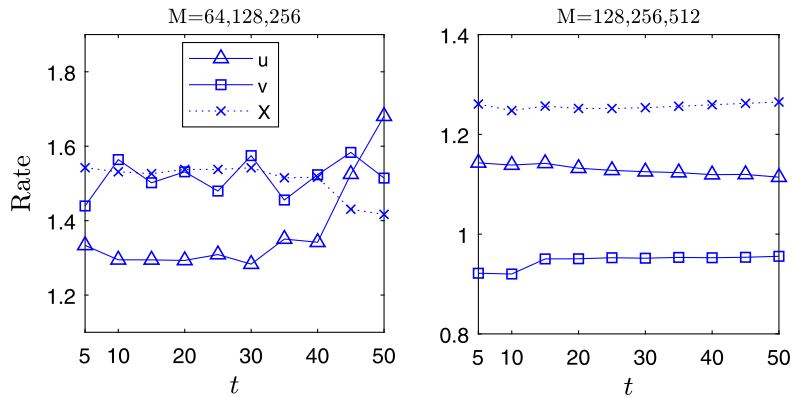


Fig. 3. The convergence rates for the fluid velocity (u, v) and the vesicle configuration \mathbf{X} . Left: $M = 64$; Right: $M = 128$.

and the dimensionless parameters are fixed by $Ca = 1$ and $Wi = 1$. We shall choose four different Cartesian grid sizes $M = 64, 128, 256, 512$ to examine convergence rates. Under shear flow $(u, v) = (y, 0)$ in the computational domain $[-8, 8]^2$, we set the parameters by $Re = 10^{-3}$, $\lambda = 2$, $\beta = 1$, $h = 16/M$, and $\Delta t = h/128$. For the vesicle interface discretization, as we double the grid size M , we need to halve the local arclength so that the number of Lagrangian markers used must be increased by a factor of two accordingly. To be consistent, one should also be careful to adjust the stiffness parameter γ_0 used in Eq. (17) for interfacial inextensibility. For this, we choose $\gamma_0 = 5 \times 10^3 M/512$, so it becomes $\gamma_0 = 5 \times 10^3$ when $M = 512$ which is used throughout Section 5.

Fig. 3 shows the convergence rates for the velocity components $\mathbf{u} = (u, v)$ and the vesicle configuration \mathbf{X} at different times up to $t = 50$. Unlike in the previous subsection, the analytic solution in this test is not available, so we compute the convergence rate by estimating the two successive maximum errors as

$$\text{Rate} = \log_2(\|u_M - u_{2M}\|_\infty / \|u_{2M} - u_{4M}\|_\infty).$$

The rates for v and \mathbf{X} are defined in a similar manner. We can see from the figure that the rates are larger than one when $M = 64, 128, 256$ and close to one when $M = 128, 256, 512$, so the average rate is around one for all variables indicating that our numerical scheme is roughly first-order accurate. This result is consistent with the IB method being first-order accurate generally.

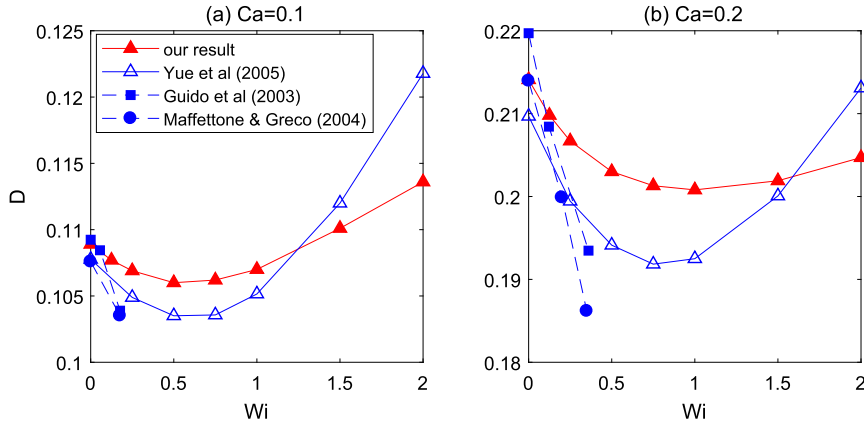


Fig. 4. Deformation parameter D of droplet in N/O fluid as a function of the Weissenberg number Wi for two Capillary numbers: (a) $Ca = 0.1$, (b) $Ca = 0.2$. Our result is compared with numerical result of Yue et al. (2005), and also with experimental data of Guido et al. (2003) and of Maffettone and Greco (2004).

4.3. Comparison of droplet deformation in N/O fluid

In the previous subsection, we have shown the convergence rates of fluid variables for a Newtonian vesicle in Oldroyd-B fluid under shear flow. In order to verify that the present numerical scheme is physically plausible, we here perform a comparison with experimental and numerical studies in literature for droplet deformation in N/O fluid under shear flow. In this test, we denote N/O fluid by a Newtonian droplet suspended in an Oldroyd-B fluid. To do this, in Eq. (3), we omit the bending force and replace the tension force by $\mathbf{F}_\gamma(\alpha, t) = -\frac{2}{Ca_d}\kappa\mathbf{n}$, where Ca_d is the capillary number associated with droplet interfacial tension and the factor 2 comes from our non-dimensionalization process. The deformation parameter is defined by $D = (L - B)/(L + B)$, where L and B are the longest and shortest lengths of the droplet measured from its center to the interface, respectively. In this test, we initially configure a circular droplet with unity radius which is centered in the computational domain $[-8, 8] \times [-4, 4]$ with the grid size 2048×1024 , as shown in Fig. 1. The number of Lagrangian markers is chosen as $N = 4096$, the uniform Eulerian mesh width is $h = 1/128$, and the time step size is $\Delta t = h/32$. We also fix the Reynolds number by $Re = 10^{-4}$ and the viscosity ratio between polymer and Newtonian solvent by $\beta = 1$, thus $\lambda = 2$.

Fig. 4 shows our numerical results on the droplet deformation as a function of the Weissenberg number Wi for two different capillary numbers $Ca = 0.1$ and 0.2 . It is also compared with experimental results [13,28] and the numerical results based on phase-field method [46]. Notice that, the experimental results are available only for small Weissenberg number. In the figure, our numerical result is quite comparable to the experiment by Guido et al. [13] for small Wi and $Ca = 0.1$, while the result of Yue et al. [46] is comparable to the one of Maffettone and Greco [28]. For small Wi and $Ca = 0.2$, our result becomes quite comparable to both experiments, while the result of Yue et al. is still comparable to the one of Maffettone and Greco. In comparison with numerical results of Yue et al., our results show slight difference but both plots of deformation parameter versus Weissenberg number show concave upward behavior as Weissenberg number increases. So we can conclude that our present numerical method is validated by simulating the Newtonian droplet in Oldroyd-B fluid. In the next section, we study on the vesicle dynamics mainly in two-phase N/O fluid under steady shear flow.

5. Numerical results and discussion

In this section, we perform numerical tests for two-dimensional vesicle dynamics under viscoelastic shear flow. To explore the effects of viscoelasticity on vesicle motions, the inner fluid is always set to be Newtonian, while the outer fluid is given by either Newtonian or non-Newtonian (Oldroyd-B). We denote these two-phase fluids by N/N and N/O, respectively. In the following subsections, we first validate our IB method by comparing with the Keller–Skalak (KS) theory in N/N fluid [21]. We then intensively investigate the viscoelastic effect on vesicle motions in N/O setting by varying the parameters such as Wi (the Weissenberg number), β (the viscosity ratio between polymer and Newtonian solvent), Re (the Reynolds number), and λ (the viscosity contrast between inner and outer fluids).

Throughout this paper, we initially configure an elliptical vesicle with the desired reduced area $\nu = 4\pi A/L^2$ by fixing the enclosed area $A = \pi$ and changing the total vesicle perimeter L . We put the vesicle under shear flow $(u, v) = (y, 0)$ in the computational domain $[-8, 8]^2$ with the grid size 512^2 , see Fig. 1. The uniform Eulerian mesh width is $h = 16/512$ and the time step size is $\Delta t = h^2/4$. The number of Lagrangian markers representing the vesicle boundary is chosen as $N = 1024$. In most cases, the numerical results are obtained up to time $t = 50$ which takes about 30 hours to finish a run using a single-core computer equipped with a CPU 3.7 GHz. Unless otherwise stated, we fix the Reynolds number by $Re = 10^{-3}$

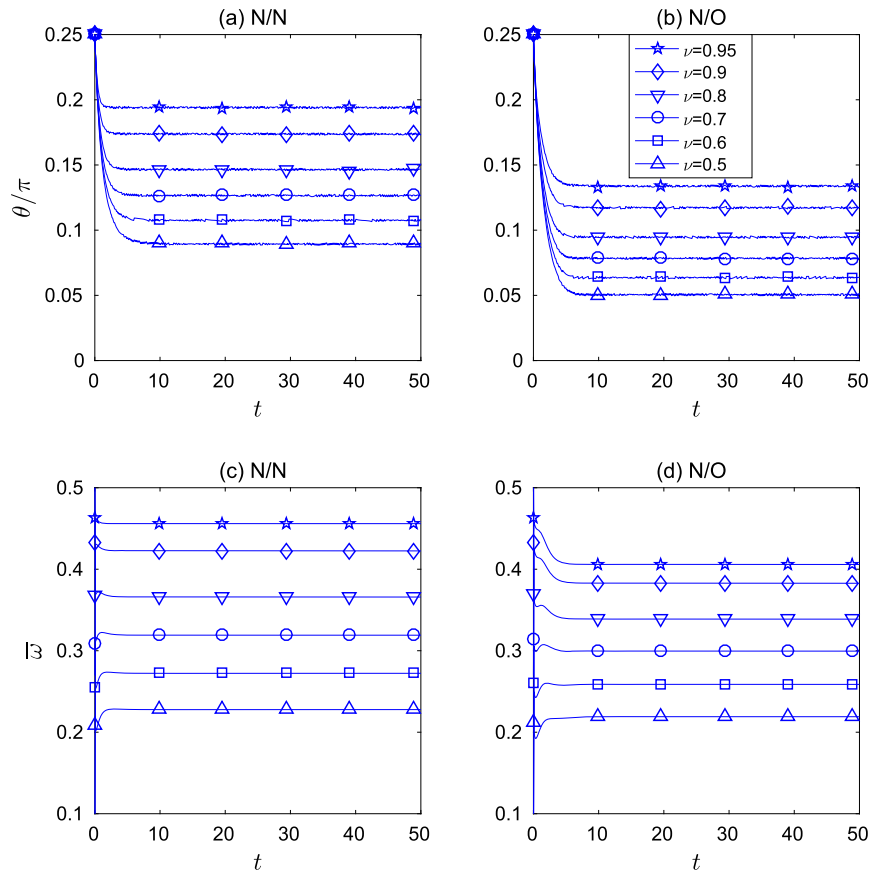


Fig. 5. Comparison of N/N (left column, (a, c)) and N/O (right column, (b, d)) cases. (a)–(b): the time evolutionary plots of inclination angle θ/π for various ν . (c)–(d) the time evolutionary plots of tank-treading frequency $\bar{\omega}$ for various ν . Here ν denotes the reduced area.

to be in Stokes regime, the capillary number by $Ca = 1$, and the viscosity ratio between polymer and Newtonian solvent by $\beta = 1$. Although mostly omitted here, we tested for different Ca ranged from 1 to 100 and initial tilt-angles 0 and $\pi/4$. Since the quantitative results associated with shear-induced vesicle TT motions are almost identical for different initial configuration of vesicle, we tilt the vesicle initially only by an angle $\theta = \pi/4$. In order to support this statement, in the next subsection, we show the time-dependent variation of inclination angle and angular frequency of tank-treading vesicle for different configurations initially tilted by 0, $\pi/8$, and $\pi/4$. The stiffness parameter used for the nearly inextensible vesicle boundary is chosen as $\gamma_0 = 5 \times 10^3$ with which the relative changes in vesicle area A and its total length L are less than 0.5% during all simulations we have performed.

For shear-induced vesicle motions in N/N fluid, two major types of motion have been well investigated; namely (1) tank-treading (TT) motion, and (2) tumbling (TB) motion. A vesicle with TT motion takes a stationary shape and constant inclination angle θ independent of time, while a vesicle with TB motion periodically rotates like a rigid body. These behaviors have been found in asymptotic theory [21] and also numerical simulations such as in [24]. Another motion called a vacillating-breathing (or trembling, swinging) is found between TT and TB states in the theory [29], the experiment [19], and numerical simulation [31]. However, here only TT and TB motions are observed since the vacillating-breathing is mainly attributed to the presence of vorticity axis in three dimensions.

5.1. Comparison of matched viscosity N/N and N/O fluids

As a first test, we examine the effect of viscoelasticity by comparing the vesicle tank-treading (TT) motion under shear flow for N/N and N/O fluids. Throughout this paper, we call the matched viscosity N/N fluid if the parameters $\lambda = 1$ and $\beta = 0$ are used in N/N fluid setup; while we call the matched viscosity N/O fluid if $\lambda = 1 + \beta$ and $\beta > 0$ in N/O fluid. In the latter case, the viscosity of Newtonian fluid matches with the total viscosity of Oldroyd-B fluid by $\mu_n = \mu_s + \mu_p$. Here we choose $\beta = 1$ and the Weissenberg number $Wi = 1$ for convenience in this study. Note that, the usage of $\beta = 1$ is quite common in other numerical studies [7,46,8]. Meanwhile, as reported in [41], the value of Wi can be measured close to 1 or even higher close to 10 in blood flow for hardened cells and through microtubes.

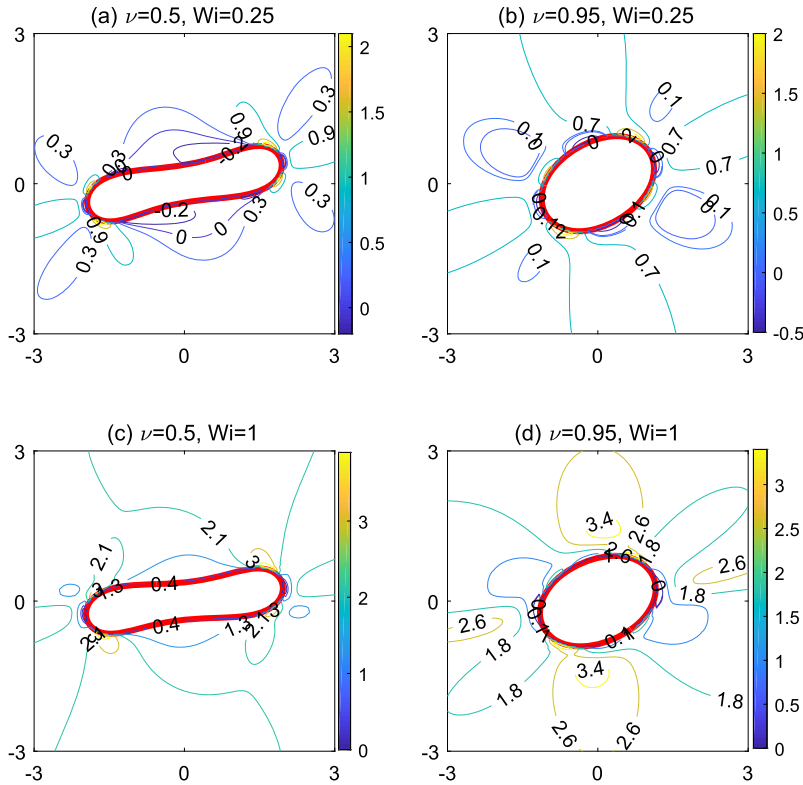


Fig. 6. Contour plot of the first normal stress difference of the polymer obtained by $H(\sigma_a - \sigma_c)$ for different Weissenberg numbers $Wi = 0.25$ and 1 . (a, c) $\nu = 0.5$; (b, d) $\nu = 0.95$, where ν is the reduced area of the vesicle drawn in a thick red line. The data is chosen at $t = 50$. (For interpretation of the colors in the figure(s), the reader is referred to the web version of this article.)

It is known that, in the case of matched viscosity N/N fluid, a vesicle under shear flow undergoes TT motion, and the inclination angle θ/π (measured by the angle between the x -axis and the longest axis of the vesicle and scaled by π) decreases as the reduced area ν decreases as shown in Fig. 5(a). One can see from Fig. 5(b) that, in the matched viscosity N/O fluid, the vesicle still undergoes TT motion and as the reduced area decreases, the angle decreases too. However, it is interesting to see that all the inclination angles in N/O fluid are significantly smaller than the ones in the case of N/N fluid due to the viscoelastic effect of Oldroyd-B fluid outside of the vesicle. A similar behavior was reported in the study of droplet deformation such as in [7]. In Table 1 of [7], for a Newtonian droplet immersed in an Oldroyd-B fluid under shear flow, it is shown that the inclination angle decreases as the Weissenberg number (or Deborah number) increases. To explain why, the authors plotted the first normal stress difference of the polymer defined by $N_1 = H(\sigma_a - \sigma_c)$ in Fig. 11 of [7] and found that the maximal regions of N_1 move away from the tip of the droplet to above the front tip and below the back tip with increasing Weissenberg number. This indicates that the polymer stress contributes to decrease the inclination angle of the droplet with increasing Wi . We believe that such explanation is also applicable to our present study on vesicle problem. Fig. 6 shows the contour plots of the first normal stress difference of the polymer N_1 for different Weissenberg numbers $Wi = 0.25$ and 1 . As we can see from this figure, when Wi increases, the maximal regions of N_1 move away from the tip of the vesicle and the overall values get higher, so the polymer stress tends to align the vesicle along the x -direction more. As a result, the inclination angle of the tank-treading vesicle decreases with increasing Wi .

For the vesicle TT motion, it is also interesting to measure the TT angular frequency as in [24]

$$\bar{\omega}(t) = 2\pi \int_{\Sigma(t)} \frac{|\mathbf{X}_\alpha|}{|\mathbf{U} \cdot \boldsymbol{\tau}|} d\alpha,$$

where $\mathbf{U} \cdot \boldsymbol{\tau}$ is the tangential component of velocity of the Lagrangian marker. Fig. 5(c) and Fig. 5(d) show the time evolutionary plots of $\bar{\omega}$ for the cases of N/N and N/O fluids, respectively. One can also see that, as the reduced area ν decreases, the TT angular frequency decreases for both N/N and N/O fluids. The frequencies in N/O fluid are comparably smaller than the ones in N/N fluid although the differences become smaller as ν decreases.

Although the viscoelasticity resists vesicle motion as shown in Fig. 5, one might wonder whether the vesicle dynamics is significantly influenced by different initial configurations of vesicle. To see this, we put a vesicle with reduced area $\nu = 0.8$ initially tilted by $\theta_0 = 0, \pi/8, \text{ and } \pi/4$ under shear flow. We also vary the Weissenberg number $Wi = 0.5, 1, 2$, but fix

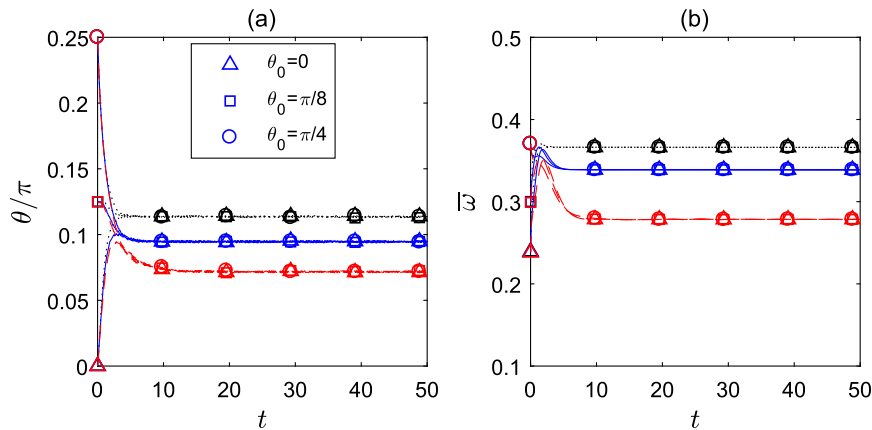


Fig. 7. The comparisons of (a) the inclination angle θ/π and (b) the average TT frequency $\bar{\omega}$ both in terms of time, for different configuration of vesicle with fixed $\nu = 0.8$ initially tilted by $0, \pi/8$, and $\pi/4$. Three different Weissenberg numbers are also chosen by $Wi = 0.5$ (black dotted lines), $Wi = 1$ (blue solid lines), and $Wi = 2$ (red dashed lines).

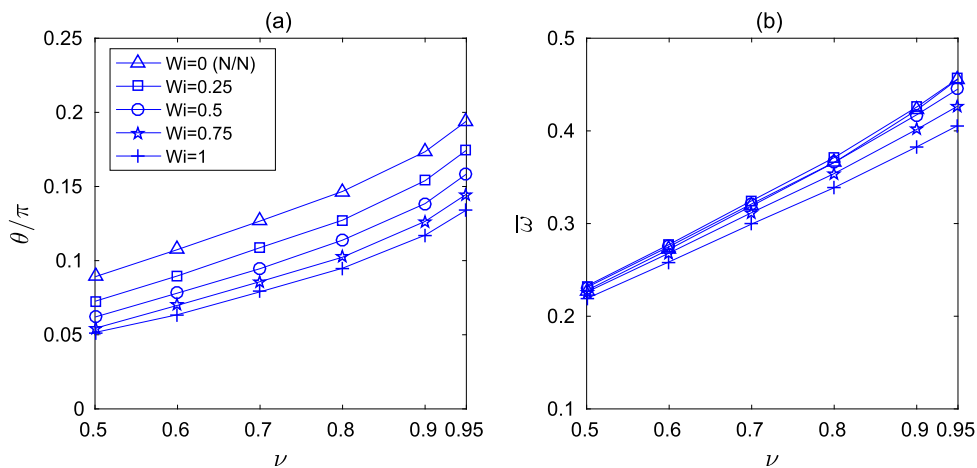


Fig. 8. For various Wi and fixed $Ca = 1$, (a) the inclination angle θ/π and (b) the average TT frequency $\bar{\omega}$ both in terms of the reduced area ν . Here Wi and Ca denote the Weissenberg number and the capillary number, respectively. The data is chosen at $t = 50$.

the capillary number $Ca = 1$. In Fig. 7, we compare the time-dependent variation of inclination angle θ/π and angular frequency $\bar{\omega}$ for these configurations. Before the onset of stationary TT regime, the suspended vesicle with $\theta_0 = 0$ rotates in the counter-clockwise direction toward stationary state, whereas that with $\theta_0 = \pi/4$ rotates in the clockwise direction. Then during stationary TT motion with constant inclination angle and tank-treading frequency, those three results with different initial configurations coincide with each other almost perfectly. So, it seems that the equilibrium TT inclination angle and the averaged angular frequency are independent of initial vesicle configurations.

5.2. Effect of Weissenberg number on TT motion

In this subsection, we investigate the effect of different Weissenberg numbers on the vesicle tank-treading motion. The computational setup is the same as in the previous subsection except we vary the Weissenberg number. As shown in Fig. 5, both inclination angle and angular frequency tend to be stationary after $t \approx 10$ so here we just mark the equilibrium values. Fig. 8(a) shows the stationary inclination angle θ/π versus the reduced area ν for different Weissenberg numbers $Wi = 0, 0.25, 0.5, 0.75, 1$. Here, $Wi = 0$ represents the case of N/N fluid. One can see that as the Weissenberg number increases, the angle θ/π decreases for all different cases of ν . It appears that the slopes are almost identical between two different ν for all values of Wi which indicates relatively constant contribution of the viscoelasticity to vesicle dynamics in TT regime. Fig. 8(b) shows a qualitatively similar trend for TT angular frequency, that is, $\bar{\omega}$ decreases with increasing Wi . However, unlike the inclination angle, the discrepancy of $\bar{\omega}$ at fixed ν is quite small, and it appears that the stronger viscoelasticity of outer fluid slows down the average TT frequency more for the swollen vesicle than the flattened one.

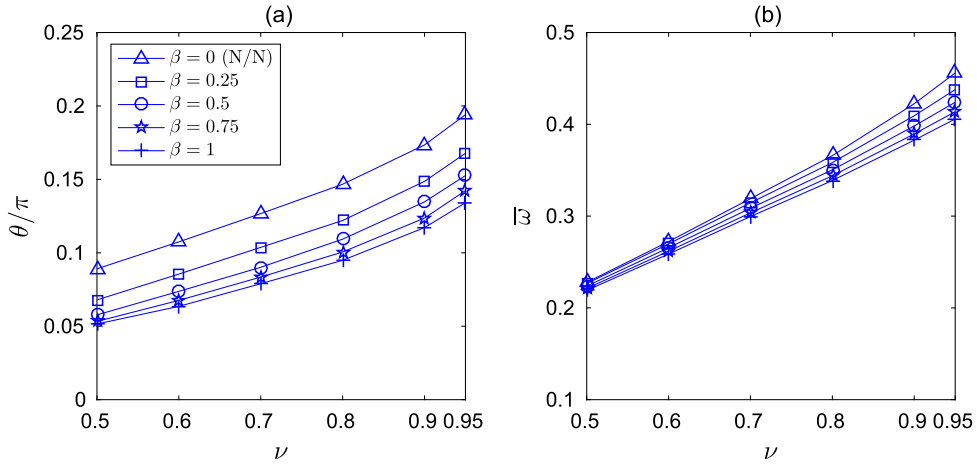


Fig. 9. For various β and fixed $Ca = 1$, (a) the inclination angle θ/π and (b) the average TT frequency $\bar{\omega}$ both in terms of the reduced area ν . Here β denotes the viscosity contrast between the polymer and the Newtonian solvent. The data is chosen at $t = 50$.

5.3. Effect of viscosity ratio between polymer and Newtonian solvent

In this subsection, we vary the viscosity ratio between polymer and Newtonian solvent which is defined by β in Eq. (20). Since we consider the matched viscosity N/O fluid here, once β is chosen, the viscosity contrast is determined by $\lambda = 1 + \beta$. This numerical experiment is closely related to the previous results tested for different Weissenberg numbers Wi . As we can see in the previous subsection, the viscoelasticity of the outer fluid tends to decrease the TT inclination angle. When $\beta = 0$, the fluid is purely Newtonian. As β increases, the viscoelastic effect of the polymer becomes larger, so the TT inclination angle decreases as we can see from Fig. 9(a). The decrement at fixed ν gets smaller as β increases linearly from 0 to 1. As shown in Fig. 9(b), the TT frequency for the swollen vesicle is affected more than for the flattened one. Such trend of the variation in TT inclination angle and frequency at equilibrium is similar to the results shown in Fig. 8 for the effect of different Weissenberg numbers, in which, instead of β , Wi increases linearly to take into account the different viscoelasticities. Thus, changing β or Wi seems to have similar effect. For the rest of this paper, we fix $\beta = 1$ but vary Wi to examine the polymer viscoelastic effect on the vesicle motion under shear flow.

5.4. Effect of Reynolds number

In most available literature, the simulations of vesicle motions under shear flow are restricted to Stokes flow by neglecting the fluid inertia. However, it was shown in [23,36] that the inertia effect can inhibit vesicle TB motion under shear flow in N/N fluid. In this subsection, we investigate the inertia effect by varying the Reynolds number Re in N/O fluid. For comparison purpose, we also show the results in N/N fluid. Fig. 10(a) and Fig. 10(b) show the inclination angle versus reduced area for the cases of N/N and N/O fluids, respectively. Here, we vary the Reynolds number from Stokes regime $Re = 10^{-3}$ to the Navier–Stokes regime $Re = 1$. One can immediately see from these two sub-figures that by increasing the Reynolds number, the inclination angle increases accordingly. Meanwhile, the inclination angles obtained from $Re = 1$ in both N/N and N/O fluids are significantly larger than the ones obtained from $Re = 10^{-3} - 10^{-1}$, which shows that the inertia does affect the vesicle dynamics under shear flow. Furthermore, since the inclination angle becomes larger when $Re = 1$, this confirms again that the inertia effect might inhibit tumbling motion as in the literature [23,36]. Fig. 10(c) and Fig. 10(d) show the average TT angular frequency $\bar{\omega}$ versus reduced area for the cases of N/N and N/O fluids, respectively. In both fluids, the frequency at $Re = 1$ are significantly smaller than the results obtained from $Re = 10^{-3} - 10^{-1}$, which once again confirms the inertia effect. It is also interesting to see that the frequency is more strongly affected by Re in N/N fluid than in N/O fluid.

5.5. Effect of viscosity contrast between inner and outer fluids

So far, we have considered the matched viscosity in N/N fluid and N/O fluid. In this subsection, we examine the effect of unmatched viscosity in both fluids. As mentioned before, we call the unmatched viscosity N/N fluid if $\lambda > 1$ and $\beta = 0$, and the unmatched viscosity N/O fluid if $\lambda > 2$ and $\beta = 1$, respectively. In the case of unmatched viscosity N/N fluid, a vesicle can undergo TB motion when the viscosity contrast reaches a critical threshold and triggers the transition from TT to TB. As discussed in Keller and Skalak (KS) theory [21], the critical viscosity contrast for the TT to TB transition can be computed by setting the stationary inclination angle to be zero. So before the transition, the stationary inclination angle decreases and remains positive as the viscosity contrast increases (but smaller than the threshold). Fig. 11(a) shows the behaviors of the inclination angle versus the viscosity contrast for different reduced area in N/N fluid. Here, the theoretical prediction of

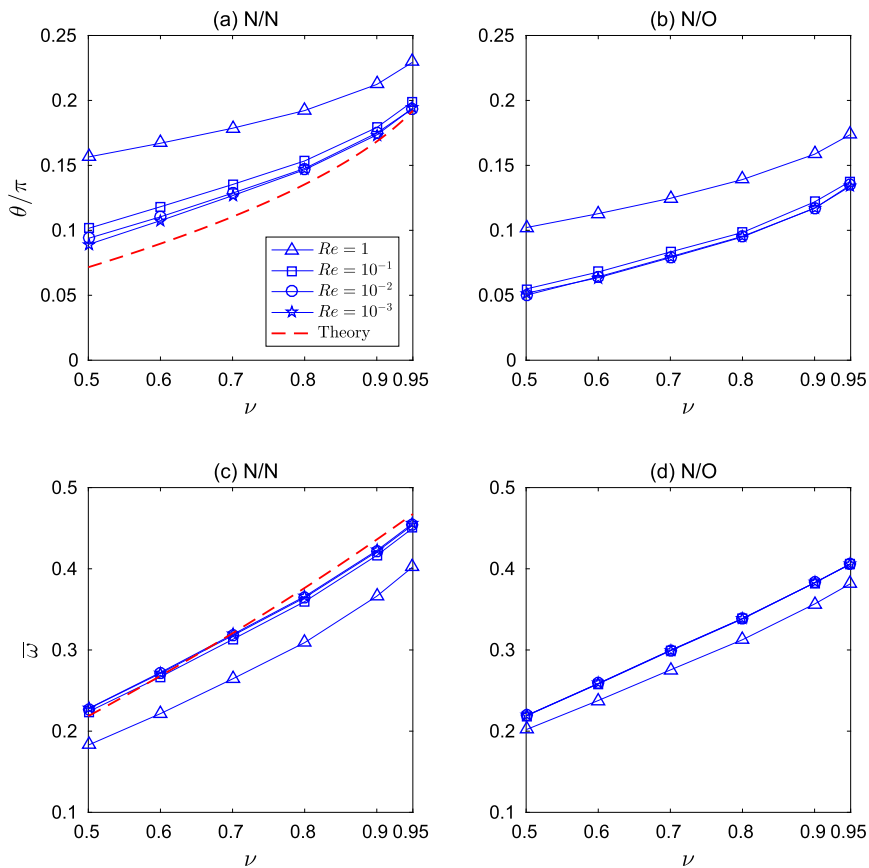


Fig. 10. For various Re and fixed $Ca = 1$, the inclination angle θ/π in (a, b); The average TT frequency $\bar{\omega}$ in (c, d). The fluid types are N/N in (a, c) and N/O with $Wi = 1$ in (b, d), respectively. The theoretical result in [24] modified for 2D case is compared with our numerical results. Here Re and Ca denote the Reynolds number and the capillary number, respectively. The data is chosen at $t = 50$.

KS theory is also plotted in this figure. One can see that although our numerical results are a little bit overestimated than the theoretical predictions which was also observed in other studies [6,22], the qualitative trend is in a good agreement. We attribute such deviations to the assumption of stationary elliptic shape used in KS theory while in our simulations, the stationary vesicle shape can be a dumbbell one especially for the cases of smaller reduced area with $Ca = 1$.

Figs. 11(b)–(d) show the stationary inclination angle θ/π versus the viscosity contrast λ before the transition from TT to TB in the case of N/O fluid for different Weissenberg numbers ($Wi = 0.5, 0.75, 1$). Here, various reduced areas are also considered. As in N/N fluid, the stationary inclination angle decreases as the viscosity contrast increases for all reduced areas. However, it is surprising to see that the stationary inclination angle becomes negative as the viscosity contrast increases but remains in TT motion. To the best of our knowledge, this is the first numerical result showing that negative stationary inclination angle exists in vesicle TT motion, which certainly is attributed to the viscoelastic effect of the surrounding fluid. Some time evolutionary snapshots of vesicle TT motion with negative inclination angle shall be given later. It is also clear to see that a vesicle can sustain TT motion even for a large λ , which is more profound at increasing Weissenberg number. Another remarkable result is that, as Wi increases, TT regime sustains with much higher λ for the flattened vesicle. In Figs. 11(b)–(d), a vesicle with large reduced area $\nu = 0.95$ tends to tumble at $\lambda = 16, 18$ and 20 for the corresponding $Wi = 0.5, 0.75$ and 1, whereas a vesicle with $\nu = 0.5$ does at $\lambda = 8, 12$, and 21 in comparison. So, in order to trigger the TT to TB transition in N/O fluid, our simulation indicates that the flattened vesicle requires even higher viscosity contrast λ than the swollen does at high Weissenberg number.

To quantify the transition from TT to TB, one can estimate the numerical critical viscosity contrast by running successive simulations. Fig. 12 plots the numerical critical viscosity contrast λ_c as a function of ν with various Wi . The critical contrast in N/N fluid obtained from KS theoretical result is also included for comparison. One can immediately see that, for fixing reduced area ν , the critical viscosity contrast λ_c increases as Weissenberg number Wi increases as shown in Figs. 11(b)–(d). Meanwhile, λ_c increases with the reduced area ν for all Weissenberg numbers $Wi = 0, 0.25, 0.5, 0.75$ except for the case of $Wi = 1$ in which λ_c behaves non-monotonically. Such non-monotonic behavior at moderate Wi is also found in droplet deformation under shear flow [46]. However, it is not clear what physical mechanisms cause such behavior or whether it is simply from the numerical limitation since we run the vesicle motions only up to time $t = 50$.

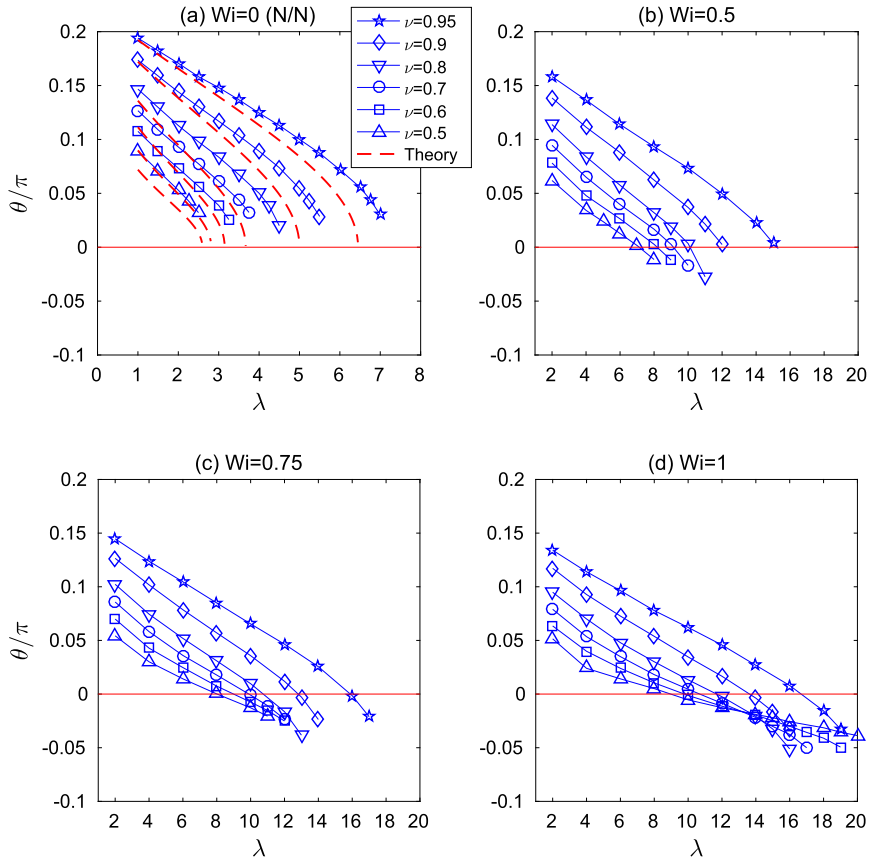


Fig. 11. The inclination angle θ/π in terms of the viscosity contrast λ for various Weissenberg number Wi . The data is chosen at $t = 50$.

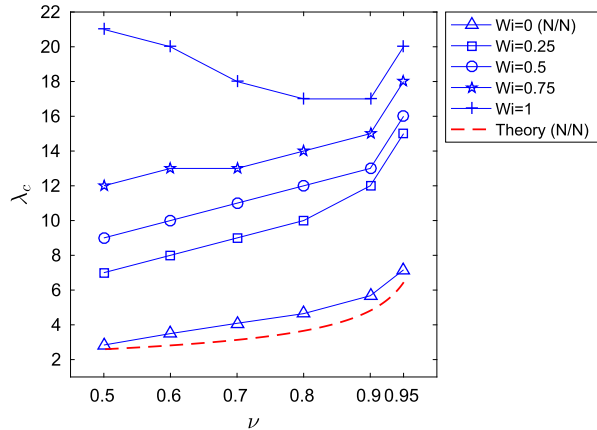


Fig. 12. The critical viscosity contrast λ_c versus the reduced area ν for various Wi and fixed Ca . Here Wi and Ca denote the Weissenberg number and the capillary number, respectively. The data is chosen at $t = 50$.

For illustration purpose, some time evolutionary snapshots of vesicle TT motion in N/O fluid are plotted in Fig. 13. In this figure, two different vesicles are considered; one is a flattened vesicle with $\nu = 0.5$ and $\lambda = 20$, and the other is a swollen vesicle with $\nu = 0.95$ and $\lambda = 19$. Shortly after the relaxation of bending, the vesicles start to rotate in a clockwise direction toward stationary state. At $t = 5$, the vesicles are almost aligned with the x -axis as shown in Fig. 13(b), and rotate more shown in Fig. 13(c) at $t = 10$. Unlike the tumbling motion in N/N fluid, these vesicles suddenly reach the stationary TT motion at negative inclination angles as shown in Figs. 13(d)–(f) and last until the end of simulation time $t = 50$, see Fig. 14. These steady values of the inclination angle are marked in Fig. 11(d).

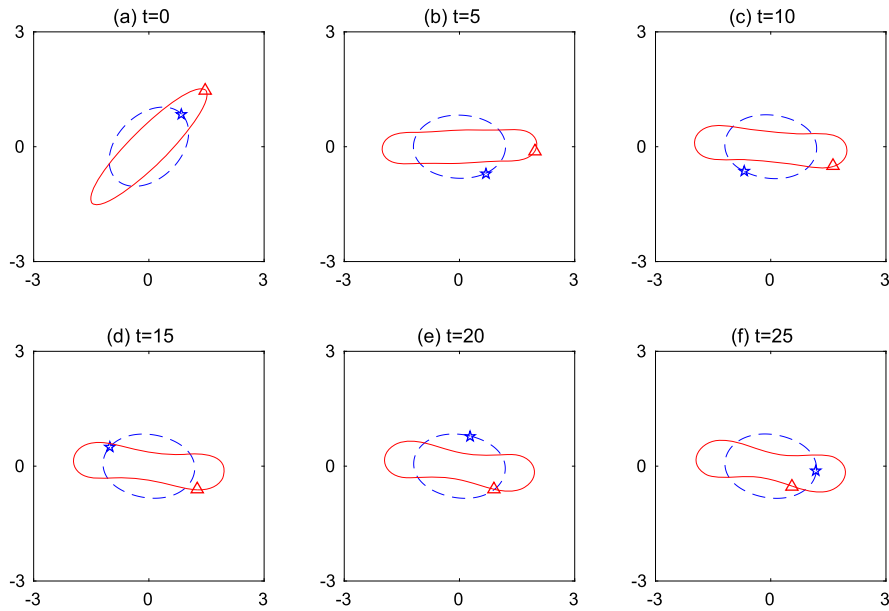


Fig. 13. Snapshots of TT vesicles with $\nu = 0.5$, $\lambda = 20$ (red solid line) and $\nu = 0.95$, $\lambda = 19$ (blue dashed line) suspended in N/O fluid with $Re = 10^{-3}$, $Ca = 1$, and $Wi = 1$. We denote the reduced area by ν , the viscosity contrast by λ , the Reynolds number by Re , the capillary number by Ca , and the Weissenberg number by Wi .

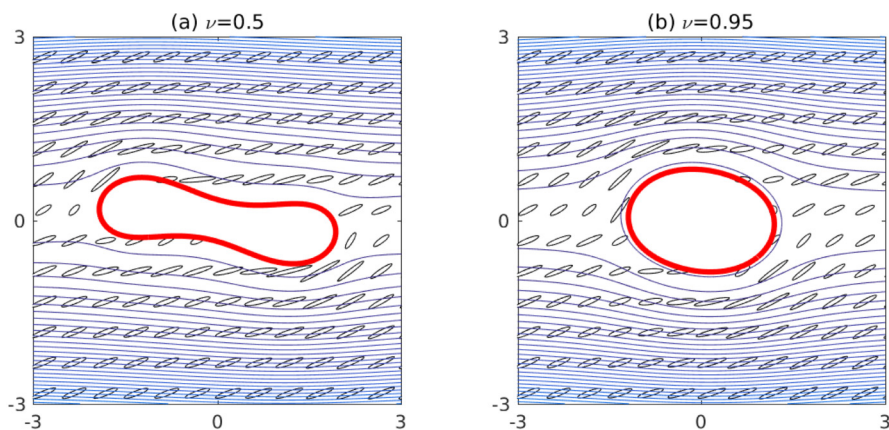


Fig. 14. Streamlines and stress-ellipses at time $t = 50$ for vesicles with (a) $\nu = 0.5$, $\lambda = 20$ and (b) $\nu = 0.95$, $\lambda = 19$ both in N/O fluid with $Re = 10^{-3}$, $Ca = 1$, and $Wi = 1$. This corresponds to Fig. 13. We denote the reduced area by ν , the viscosity contrast by λ , the Reynolds number by Re , the capillary number by Ca , and the Weissenberg number by Wi .

According to [34,46], viscoelastic effect on a suspended droplet dynamics comes not only from the polymer stress directly, but also from the flow modified by the stress. To understand the viscoelastic effect on vesicle tank-treading motion at negative inclination angle in N/O fluid, we plot flow streamlines and stress-ellipses for two vesicles at $t = 50$ shown in Fig. 14. The stress-ellipse visualizes the eigenvalues and eigenvectors of a dimensionless conformation tensor $\bar{\sigma} = (Wi/\beta)\sigma + \mathbf{I}$ as shown in [8]. For a stress-ellipse, the semi-major axis is aligned with the eigenvector corresponding to the maximal eigenvalue of $H\bar{\sigma}$ and its length is scaled proportionally to the eigenvalue. Similarly, the semi-minor axis is defined with the eigenvector corresponding to the minimal eigenvalue. The Oldroyd-B model can be derived from a molecular model of suspended Hookean dumbbells in a Newtonian solvent [32, Ch 2.6.1], so an ellipse physically indicates how an ensemble average of elastic dumbbells (bead-spring structures or coils) is immersed in fluid. These stress-ellipses nearby the vesicle boundary illustrated in the figure are quite elongated parallel to the streamline, so the dumbbells are aligned predominantly parallel to the streamline yielding an anisotropic contribution to flow field. Thus, the biased polymer stress and the fluid flow modified by the stress affect the vesicle TT inclination angle to be lower as seen in Subsection 5.2.

To see more about the polymer contribution in the presence of viscosity contrast, we plot the contour of the first normal stress difference of the polymer in Fig. 15. Unlike shown in Figs. 6(c, d), the maximal regions of the stress difference move away from the tip of vesicle in the opposite directions, that is, to below the front tip and above the back tip. Our perception

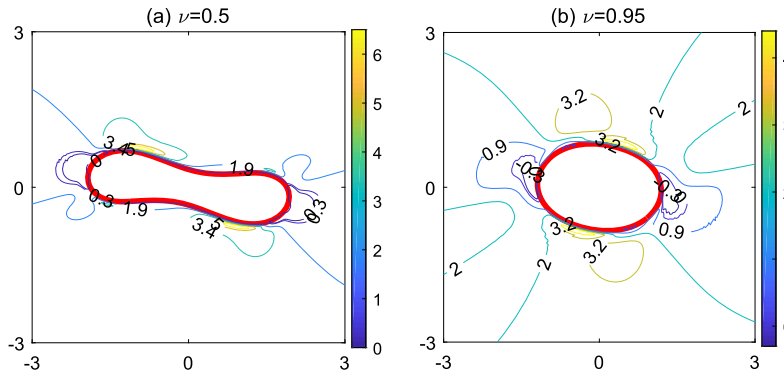


Fig. 15. Contour plot of the first normal stress difference of the polymer obtained by $H(\sigma_a - \sigma_c)$ for fixed Weissenberg number $Wi = 1$. Here ν is the reduced area of the vesicle. This figure corresponds to Fig. 14.

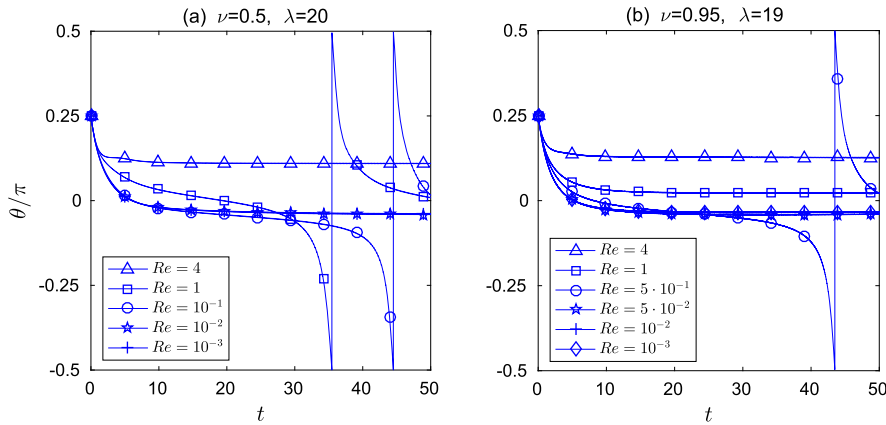


Fig. 16. The time evolution of inclination angle for vesicles with (a) $\nu = 0.5, \lambda = 20$ and (b) $\nu = 0.95, \lambda = 19$ in unmatched viscosity N/O fluid with $Ca = 1$ and $Wi = 1$. We denote the reduced area by ν , the viscosity contrast by λ , the Reynolds number by Re , the capillary number by Ca , and the Weissenberg number by Wi .

is that the polymer stress seems to align the vesicle along the x -direction, while the unmatched viscosity stress seems to make the vesicle tumble. So the counter effect between those two stresses makes the vesicle tank-tread at negative inclination angle. Certainly, some experimental and theoretical studies should be conducted to verify our findings in the near future.

5.6. Study on Reynolds number in unmatched viscosity N/O fluid

In unmatched viscosity N/N fluid, it is known that the TB motion is inhibited by inertia effect and the steady TT inclination angle increases with increasing Re [23,36]. As the last numerical experiment, we study the inertia effect by putting a vesicle into unmatched viscosity N/O fluid. Fig. 16 shows the time evolutionary plots of inclination angles for two different vesicles; a flattened vesicle with $\nu = 0.5$ and $\lambda = 20$ in Fig. 16(a) and a swollen vesicle with $\nu = 0.95$ and $\lambda = 19$ in Fig. 16(b). For the flattened vesicle case in Fig. 16(a), the TT inclination angle is negative in Stokes regime when $Re = 10^{-3}$ and 10^{-2} as mentioned before. However, as the Reynolds number increases to $Re = 10^{-1}$ and 1, the flattened vesicle starts to tumble, and it tumbles faster as Re increases. As we increase the Reynolds number to $Re = 4$, it is striking to see that the vesicle abruptly tank-treads at a positive inclination angle. This interesting behavior has also been observed in the swollen vesicle in Fig. 16(b). For the swollen vesicle case, the TT inclination angle is negative in Stokes regime when $Re = 10^{-3}$, 10^{-2} , and $5 \cdot 10^{-2}$. As we increase the Reynolds number to $Re = 5 \cdot 10^{-1}$, the swollen vesicle tumbles. As we increase further to $Re = 1$, the vesicle suddenly tank-treads at a positive inclination angle, and at the higher $Re = 4$, the larger positive TT inclination angle is found. From those simulation results, one can conclude that both viscoelasticity and inertia have significant effects on the vesicle dynamics in unmatched viscosity N/O fluid.

The above result can be considered as a combination of the results already observed in Fig. 10 and Fig. 11. When the viscoelasticity and the viscosity contrast dominate the vesicle dynamics as shown in Fig. 11, the vesicle undergoes tank-treading motion with negative inclination angle. As Re increases, the inertia triggers the vesicle to tumble due to the negative inclination angle. As Re further increases, the tumbling motion with higher angular frequency can occur. For the moderate Re as shown in Fig. 10, the vesicle in turn undergoes the tank-treading motion with positive inclination angle.

As Re even gets higher, the positive inclination angle gets larger to be aligned along the shear flow direction, so the angle increases to the limit $\pi/4$.

6. Conclusions

The Newtonian vesicle dynamics in viscoelastic Oldroyd-B fluid (denoted by N/O) under shear flow has been extensively investigated in this paper. We first formulate the problem in an immersed boundary framework and then present the step-by-step numerical algorithm. As a first validation to our Oldroyd-B fluid solver, we devise an analytical solution to the problem and check the numerical accuracy. We then perform a series of numerical experiments. For matched or unmatched viscosity in N/N or N/O fluid, the numerical results can be summarized as follows.

- The inclination angle and tank-treading frequency of the N/O fluid case are comparably smaller than the ones in N/N fluid.
- In matched viscosity N/O fluid, the vesicle inclination angle in TT regime decreases with increasing Weissenberg number.
- In unmatched viscosity N/O fluid, the inclination angle decreases even more as the viscosity contrast increases, and most surprisingly, the negative inclination angle is found in TT regime, indicating that the viscoelasticity of outer fluid tends to lag the tumbling motion.
- TT motion with negative inclination angle is clearly observed for the flattened vesicles in N/O fluid with moderate Weissenberg number.
- The vesicle tank-treads at negative inclination angle at small Reynolds number, then abruptly tumbles at slightly higher Reynolds number, and eventually returns to tank-tread at positive inclination angle at even higher Reynolds number.

In conclusion, this interplay between the viscoelasticity and the viscosity contrast is quite interesting and worths further investigations through theory and experiments. Meanwhile, the scheme should be able to extend to 3D based on our previous work on 3D immersed boundary simulations for vesicle dynamics in N/N fluid [35]. The remaining numerical challenges are still to improve the calculation of bending force and the handling of surface mesh distortion occurred in simulations. We will leave the 3D simulations for Newtonian vesicles in viscoelastic fluid to the future work.

Acknowledgements

The work of M.-C. Lai was supported in part by Ministry of Science and Technology of Taiwan under research grant MOST-104-2115-M-009-014-MY3 and NCTS. Y. Kim was supported by National Research Foundation of Korea Grant (2017R1E1A1A03070636).

References

- [1] D. Abreu, M. Levant, V. Steinberg, U. Seifert, Fluid vesicles in flow, *Adv. Colloid Interface Sci.* 208 (2014) 129–141.
- [2] Y. Bao, J. Kaye, C.S. Peskin, A Gaussian-like immersed-boundary kernel with three continuous derivatives and improved translational invariance, *J. Comput. Phys.* 316 (2016) 139–144.
- [3] J.T. Beale, Partially implicit motion of a sharp interface in Navier–Stokes flow, *J. Comput. Phys.* 231 (2012) 6159–6172.
- [4] T. Biben, A. Farutin, C. Misbah, Three-dimensional vesicles under shear flow: numerical study of dynamics and phase diagram, *Phys. Rev. E* 83 (2011) 031921.
- [5] J.W. Barrett, H. Garcke, R. Nürnberg, Numerical computations of the dynamics of fluidic membranes and vesicles, *Phys. Rev. E* 92 (2015) 052704.
- [6] J. Beaucourt, F. Rioual, T. Séon, T. Biben, C. Misbah, Steady to unsteady dynamics of a vesicle in a flow, *Phys. Rev. E* 69 (2004) 011906.
- [7] T. Chinyoka, Y.Y. Renardy, M. Renardy, D.B. Khismatullin, Two-dimensional study of drop deformation under simple shear for Oldroyd-B liquids, *J. Non-Newton. Fluid Mech.* 130 (2005) 45–56.
- [8] J.C. Christell, R. Cortez, D.B. Khismatullin, L.J. Fauci, Shape oscillations of a droplet in an Oldroyd-B fluid, *Physica D* 240 (2011) 1593–1601.
- [9] S. Chien, S. Usami, R.J. Dellenback, M.I. Gregersen, Shear-dependent deformation of erythrocytes in rheology of human blood, *Am. J. Physiol.* 219 (1970) 136–142.
- [10] J. Deschamps, V. Kantsler, E. Segre, V. Steinberg, Dynamics of a vesicle in general flow, *Proc. Natl. Acad. Sci. USA* 106 (2009) 11444–11447.
- [11] A. Farutin, C. Misbah, Squaring, parity breaking, and S tumbling of vesicles under shear flow, *Phys. Rev. Lett.* 109 (2012) 248106.
- [12] J.L. Guermond, P. Mineev, J. Shen, An overview of projection methods for incompressible flows, *Comput. Methods Appl. Mech. Eng.* 195 (2006) 6011–6045.
- [13] S. Guido, M. Simeone, F. Greco, Deformation of a Newtonian drop in a viscoelastic matrix under steady shear flow: experimental validation of slow flow theory, *J. Non-Newton. Fluid Mech.* 114 (2003) 65–82.
- [14] W.-X. Huang, C.B. Chang, H.J. Sung, Three-dimensional simulation of elastic capsules in shear flow by the penalty immersed boundary method, *J. Comput. Phys.* 231 (2012) 3340–3364.
- [15] W.-F. Hu, Y. Kim, M.-C. Lai, An immersed boundary method for simulating the dynamics of three-dimensional axisymmetric vesicles in Navier–Stokes flows, *J. Comput. Phys.* 257 (2014) 670–686.
- [16] F.H. Harlow, J.E. Welsh, Numerical calculation of time-dependent viscous incompressible flow of fluid with a free surface, *Phys. Fluids* 8 (1965) 2181–2189.
- [17] D. Izbassarov, M. Muradoglu, A front-tracking method for computational modeling viscoelastic two-phase flow systems, *J. Non-Newton. Fluid Mech.* 223 (2015) 122–140.
- [18] V. Kantsler, V. Steinberg, Orientation and dynamics of a vesicle in tank-treading motion in shear flow, *Phys. Rev. Lett.* 95 (2005) 258101.
- [19] V. Kantsler, V. Steinberg, Transition to tumbling and two regimes of tumbling motion of a vesicle in shear flow, *Phys. Rev. Lett.* 96 (2006) 036001.
- [20] V. Kantsler, E. Segre, V. Steinberg, Critical dynamics of vesicle stretching transition in elongational flow, *Phys. Rev. Lett.* 101 (2008) 048101.
- [21] S.R. Keller, R. Skalak, Motion of a tank-treading ellipsoidal particle in a shear flow, *J. Fluid Mech.* 120 (1982) 27–47.

- [22] Y. Kim, M.-C. Lai, Simulating the dynamics of inextensible vesicles by the penalty immersed boundary method, *J. Comput. Phys.* 229 (2010) 4840–4853.
- [23] Y. Kim, M.-C. Lai, Numerical study of viscosity and inertial effects on tank-treading and tumbling motions of vesicles under shear flow, *Phys. Rev. E* 86 (2012) 066321.
- [24] M. Kraus, W. Wintz, U. Seifert, R. Lipowsky, Fluid vesicles in shear flow, *Phys. Rev. Lett.* 77 (1996) 3685–3688.
- [25] V.V. Lebedev, K.S. Turitsyn, S.S. Vergeles, Dynamics of nearly spherical vesicles in an external flow, *Phys. Rev. Lett.* 99 (2007) 218101.
- [26] D.-V. Le, S.T. Wong, A front-tracking method with Catmull–Clark subdivision surfaces for studying liquid capsules enclosed by thin shells in shear flow, *J. Comput. Phys.* 230 (2011) 3538–3555.
- [27] Z.Y. Luo, S.Q. Wang, L. He, F. Xu, B.F. Bai, Inertia-dependent dynamics of three-dimensional vesicles and red blood cells in shear flow, *Soft Matter* 9 (2013) 9651–9660.
- [28] P.L. Maffettone, F. Greco, Ellipsoidal drop model for single drop dynamics with non-Newtonian fluids, *J. Rheol.* 48 (2004) 83–100.
- [29] C. Misbah, Vacillating breathing and tumbling of vesicles under shear flow, *Phys. Rev. Lett.* 96 (2006) 028104.
- [30] S. Mukherjee, K. Sarkar, Viscoelastic drop falling through a viscous medium, *Phys. Fluids* 23 (2011) 013101.
- [31] H. Noguchi, G. Gompper, Swinging and tumbling of fluid vesicles in shear flow, *Phys. Rev. Lett.* 98 (2007) 128103.
- [32] R.G. Owens, T.N. Phillips, *Computational Rheology*, Imperial College Press, London, 2002.
- [33] S.B. Pillapakam, P. Singh, A level-set method for computing solutions to viscoelastic two-phase flow, *J. Comput. Phys.* 174 (2001) 552–578.
- [34] S. Ramaswamy, L.G. Leal, The deformation of a viscoelastic drop subjected to steady uniaxial extensional flow of a Newtonian fluid, *J. Non-Newton. Fluid Mech.* 85 (1999) 127–163.
- [35] Y. Seol, W.-F. Hu, Y. Kim, M.-C. Lai, An immersed boundary method for simulating vesicle dynamics in three dimensions, *J. Comput. Phys.* 322 (2016) 125–141.
- [36] D. Salac, M.J. Miksis, Reynolds number effects on lipid vesicles, *J. Fluid Mech.* 711 (2012) 122–146.
- [37] L. Shi, T.-W. Pan, R. Glowinski, Three-dimensional numerical simulation of red blood cell motion in Poiseuille flows, *Int. J. Numer. Methods Fluids* 76 (2014) 397–415.
- [38] K. Sarkar, W.R. Schowalter, Deformation of a two-dimensional viscoelastic drop at non-zero Reynolds number in time-periodic extensional flows, *J. Non-Newton. Fluid Mech.* 95 (2000) 315–342.
- [39] G.B. Thurston, Frequency and shear rate dependence of viscoelasticity of human blood, *Biorheology* 10 (1973) 375–381.
- [40] G.B. Thurston, Rheological parameters for the viscosity, viscoelasticity and thixotropy of blood, *Biorheology* 16 (1979) 149–162.
- [41] G.B. Thurston, N.M. Henderson, Effects of flow geometry on blood viscoelasticity, *Biorheology* 43 (2006) 729–746.
- [42] L.N. Trefethen, *Spectral Methods in MATLAB*, SIAM, Philadelphia, 2000.
- [43] G. Tryggvason, R. Scardovelli, S. Zaleski, *Direct Numerical Simulations of Gas–Liquid Multiphase Flows*, Cambridge University Press, 2011.
- [44] S.K. Veerapaneni, D. Gueyffier, D. Zorin, G. Biros, A numerical method for simulating the dynamics of 3D axisymmetric vesicles suspended in viscous flows, *J. Comput. Phys.* 228 (2009) 7233–7249.
- [45] A. Yazdani, P. Bagchi, Three-dimensional numerical simulation of vesicle dynamics using a front-tracking method, *Phys. Rev. E* 85 (2012) 056308.
- [46] P. Yue, J.J. Feng, C. Liu, J. Shen, Viscoelastic effects on drop deformation in steady shear, *J. Fluid Mech.* 540 (2005) 427–437.
- [47] H. Zhao, E.S.G. Shaqfeh, The dynamics of a vesicle in simple shear flow, *J. Fluid Mech.* 674 (2011) 578–604.